Numerical investigation of three-dimensional effects during dynamic stall

M. Costes, F. Richez, A. Le Pape, R. Gavériaux

ONERA, The French Aerospace Lab
F-92190 Meudon, France

Abstract

The numerical simulation of dynamic stall around a 3D finite-span oscillating wing is compared to experimental results obtained in the Onera F2 wind-tunnel. Two turbulence models are tested, the Spalart-Allmaras model and the k-ω model. While the first of them strongly underestimates dynamic stall, the k-ω model provides a reasonably good description of 3D dynamic stall.

Introduction

Dynamic stall is one of the most difficult aerodynamic problems encountered on helicopter rotors. Its origin lies in the dissymmetry between the advancing and the retreating blade in forward flight. The lateral trim of the helicopter requires decreasing the blade pitch angle on the advancing blade and increasing it on the retreating blade. When the forward speed or the load factor of the helicopter is high enough, the retreating blade is led to operate above its static stall angle, this condition being met by the blades once per revolution. Dynamic stall allows the blade to increase its maximum lift capabilities with respect to static stall, but it also induces large negative pitching moments and consequently strong pitch-link and vibratory loads, thus limiting the flight domain of the helicopter.

The quest for improving rotor performance and for reducing helicopter operation cost may rapidly lead helicopter designers to be confronted to dynamic stall problems, e.g. at high speed or at reduced rotor RPM. It is thus necessary to better understand the complex physics of dynamic stall and to develop numerical simulation capabilities of sufficient fidelity in order to master stall-induced problems in the rotorcraft design. Indeed, numerous fundamental problems are raised by dynamic stall, such as flow separation on a smooth surface, laminar-turbulent transition by instabilities or laminar separation bubble, unsteady and turbulent separated flows, etc. At Onera, two internal research projects have been devoted to dynamic stall during the last decade, in cooperation with the German aerospace research centre DLR. The goal of these activities was to develop a better knowledge of dynamic stall phenomena together with the capability to simulate them, in order to be able to develop the techniques to control this configuration, by means of active or passive devices, afterwards [1] [2] [3] [4] [5].

In this research, detailed wind-tunnel testing of the OA209 airfoil under dynamic stall conditions was performed in the Onera low-speed F2 wind-tunnel. These series of tests have allowed to measure the pressure, velocity field, skin-friction around several static and oscillating models allowing the Reynolds number and reduced frequency to vary. Most of the tests were performed for 2D flow conditions, the wing covering the full span between the wind-tunnel walls. Some of them also concerned a 3D wing in order to investigate finite-span effects on dynamic stall, for different sweep angles.

Up to now, only the 2D airfoil test data have been used to validate CFD methods at dynamic stall. The results obtained so far have shown the importance of taking into account transition effects in the RANS models in order to predict the onset of stall correctly. Nevertheless, when massive flow

separation is obtained, too strong dynamic stall vortices are shed from the boundary layer of the airfoil, so that the negative pitching moment is significantly overestimated by the numerical predictions. As a matter of fact, flow separation is known to generate three-dimensional effects, and it is important to see how much this may affect flow prediction capabilities. This is the topic of the present paper.

Overview of work

The main objective of this work is to compare 3D finite-span oscillating wing computations with the experimental data obtained in F2 for dynamic stall conditions. This is the first time such kind of simulation is performed at Onera, due to the large computer resources requested for that.

The computation of 3D dynamic stall is indeed quite uncommon in the literature. For realistic Reynolds numbers, first comparisons between CFD analysis and the experimental data of Piziali were presented by Ekaterinaris [6]. However, the coarse mesh used at that time, the moderate stall configuration considered and the availability of surface pressure data only for comparison gave limited information about the specificities of dynamic stall for a 3D finite-span oscillating wing. The work of Spentzos et al [7] [8] about 10 years later made a significant step forward on this problem, although the number of mesh points used in the computations was still moderate according to nowadays standards. In this series of work, several wing planforms were tested and the 3-dimensional structure of the flowfield was investigated. The interaction between the dynamic stall vortex and the wing tip vortex was more particularly emphasized in this work, showing good qualitative agreement with experiment. For the last years, numerical research activities in 3D dynamic stall have also concerned rotor applications, more especially in the US with the UH-60 flight tests database [9] [10] [11] [12]. All the published work show good qualitative simulation of the dynamic stall phenomena on a rotating helicopter blade. However, this assessment relies on blade surface and integrated data (integrated pressure, rotor loads, …) only, giving therefore limited insight into the details of the dynamic stall mechanisms in this complex environment.

In the present work, an oscillating wing of constant chord and airfoil section (OA209), of aspect ratio equal to 2.78 was computed for the following pitch oscillation: $\alpha = 17° + 5° \sin \omega t$, which provides dynamic stall on the wing. The Reynolds number based on the wing chord is equal to 1 Million, the freestream Mach number to 0.16, and the reduced frequency of the oscillations, based on the semi-chord, is equal to 0.1. In the F2 experiment, 4 wing sections were instrumented, located at 50%, 80%, 95% and 99% of the wing span, with 28 Kulite unsteady pressure transducers for each section. Additionally, 8 accelerometers were set inside the wing model in order to check the accuracy of the wing oscillatory motion. Field velocity measurements were also completed for this case, giving the 3 components of the phase-averaged velocity vector in a plane located at the spanwise station r/R=80% using LDV, and in 3 planes parallel to the pitch axis located at x/c=25%/50%/75% using PIV. This set of data thus constitutes a fairly detailed database for CFD code validation. A view of the wing model in the wind-tunnel is shown in Figure 1.

Figure 1: View of the OA209 wing model in the F2 wind-tunnel

Numerical method

The CFD method used in the present work is the elsA multi-purpose software of Onera for aerodynamics [13]. It solves the Euler/RANS equations for structured multi-block grids in a finite-volume approach. For space discretization, among the various numerical schemes available, the upwind AUSM+(P) scheme developed by Edwards and Liou was selected for the inviscid part of the fluxes, mainly because of its low

numerical dissipation in the boundary layer. On the other hand, the viscous fluxes use a classical centred formulation. A second-order implicit time-discretization method is applied, with LU factorization and Newton iterations to converge the nonlinear system at each time step. A wide range of turbulence models are available in elsA, from algebraic models via one-equation and two-equation as well as Reynolds stress models up to DES. In the present work, only two models are considered: the one-equation Spalart-Allmaras and the two-equation k-ω model with Kok cross-derivative terms and the SST correction. Finally, although the 2D studies of dynamic stall have shown the large influence of laminar-turbulent transition on the flow separation and reattachment at low-speed [3], the present work only considers fully turbulent flow as a first step of 3D dynamic stall modelling.

The multiblocks structured grid used in the present study was generated with ICEM-CFD Hexa, with the following criteria in terms of mesh resolution at the wall: chordwise direction $\Delta x^+ \leq 300$, normal direction $\Delta y^+ \leq 0.6$, spanwise direction $\Delta z^+ \leq 2000$. The grid also includes between 30 and 40 points in the attached boundary layer, which can be considered as a minimum for an accurate RANS resolution. The total number of points is slightly above 17 Millions. A view of the mesh topology is presented in Figure 2. It extends from the wing root up to 5.66 spans (approximately 15.4 chords) and 20 chords in the other space directions. A C-topology around the wing allows clustering the points in the boundary layer and wake, with an O-topology around the wing tip. The other mesh blocks are of H-type. A view of the surface mesh in the vicinity of the tip is plotted in Figure 3. The O-mesh around the tip as well as the fineness of the surface mesh can be noted. The main goal is to capture the tip vortex as properly as possible, in order to simulate the finite-span effect on dynamic stall.
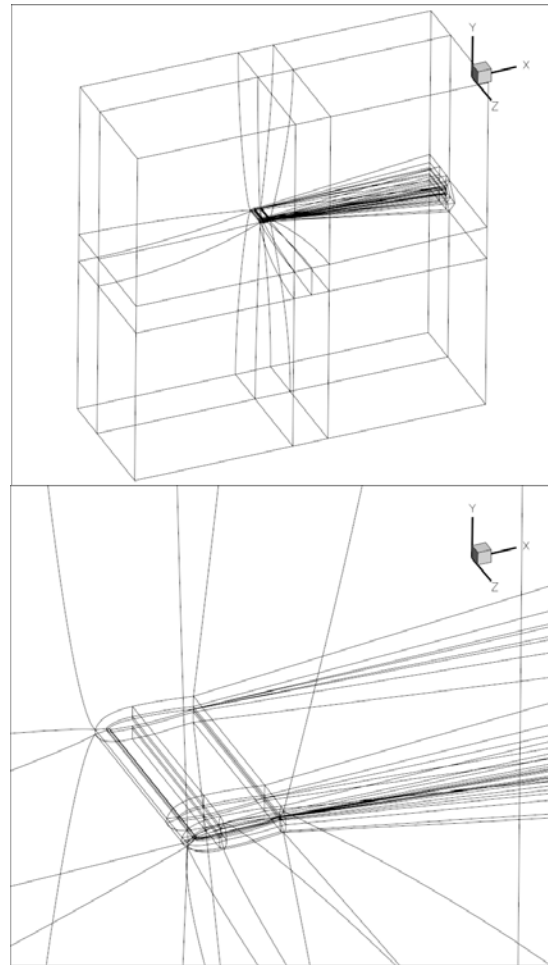

Figure 2: View of the mesh topology

The grid is split into 85 blocks distributed over 64 processors of the Titane Bull server at CCRT, under GENCI funding. A number of 18,000 time steps per period is used for the present computations, using the Gear iterative method with backward second-order time discretisation. The number of Newton iterations at each time step varied between 20 and 35, the largest number of iterations being used at least for the last cycle in order to reduce linearization errors in the results presented below.
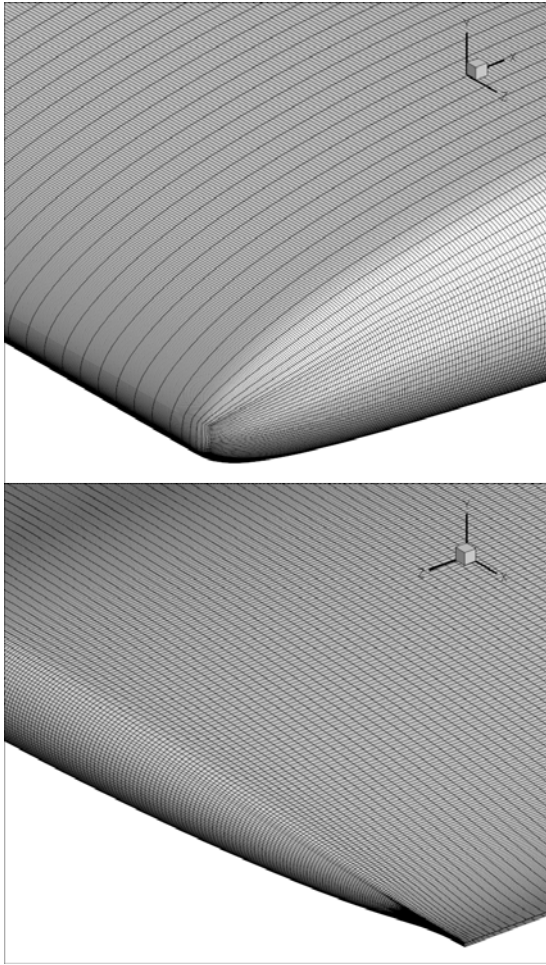
Figure 3: View of the surface mesh in the wing tip region

Results

Introduction

One of the difficulties related to large unsteady computations is the data processing. Indeed, a large number of data is generated and it is not possible to store the whole data for post-processing. The strategy adopted in the present work was to store periodically the data (every 6° of phase of the motion, corresponding to 60 times of storage during one period of oscillation). The field data was processed afterwards using the Zeppelin post-processor initially developed for processing unsteady turbomachinery data at Onera (https://elsa.onera.fr/ExternFiles/wkshp260608/5.1.pdf). Finally, for the last period computed, on-line data extraction for a limited number of quantities was performed using Python modules based on the

Cassiopée data processing tools (http://elsa.onera.fr/Cassiopee/Userguide.html).

SA turbulence model

The convergence of the integrated lift and pitching moment along the computed cycles with the Spalart-Allmaras model is presented in Figure 4 and Figure 5 respectively for 2 selected sections on the wing. At the exception of the first cycle, both lift and moment coefficients do not vary significantly from cycle to cycle. The largest difference is obtained on the pitching moment for the last cycle computed, which is due to increasing the number of Newton iterations from 20 to 35, indicating a dependence of the solution on the time discretization. Nevertheless, this dependence is weak and the last cycle can be considered as reasonably well converged in time.
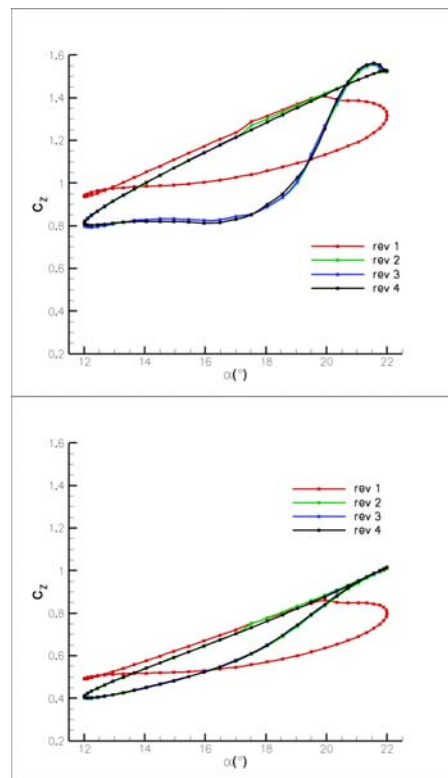

Figure 4: Convergence of the lift coefficient at two wing sections (r/R=50% - top and r/R=95% - bottom) with the SA model

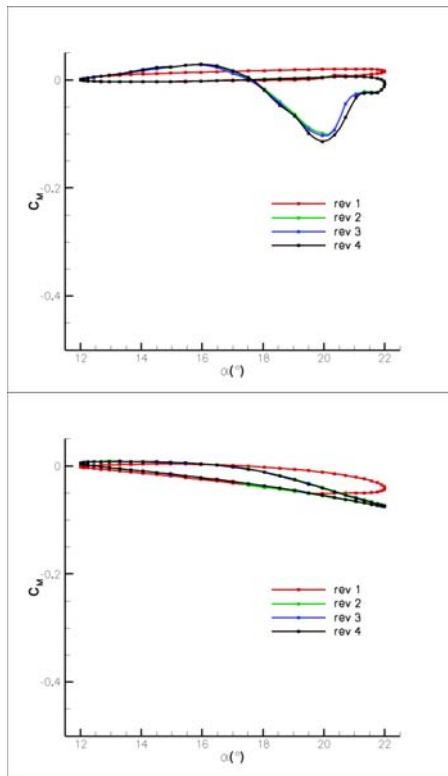**Figure 5: Convergence of the pitching moment coefficient at two wing sections (r/R=50% - top and r/R=95% - bottom) with the SA model**

A comparison of the computed lift coefficient with experiment for the 4 instrumented sections is presented in Figure 6. The experimental data was obtained by pressure integration. A clear shift is noticeable between the computed and the experimental lift coefficient, as well as a lift curve slope difference during the upstroke. As a matter of fact, it is very likely that the experimental pressures (not shown here) suffer from discrepancies in the trailing edge region, thus spoiling the pressure integration and leading to an underestimation of the lift coefficient. This will have to be corrected. Nevertheless, the comparison between computation and experiment indicates that the SA simulation only predicts dynamic stall for the innermost instrumented section, contrary to the experimental data showing lift hysteresis up to the spanwise section r/R=95%. The suction effect of the tip vortex, which increases both the lift and the lift curve slope at r/R=99% is qualitatively well predicted.
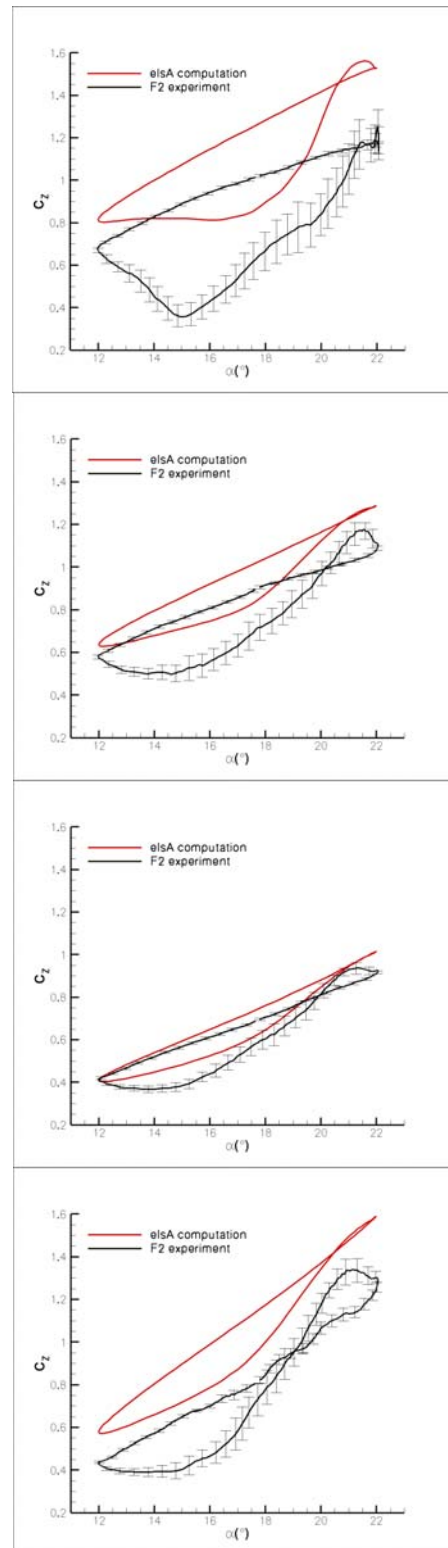
Figure 6: Evolution of the lift coefficient for the 4 instrumented wing sections (from top to bottom: 50%, 80%, 95% and 99%) – SA computation
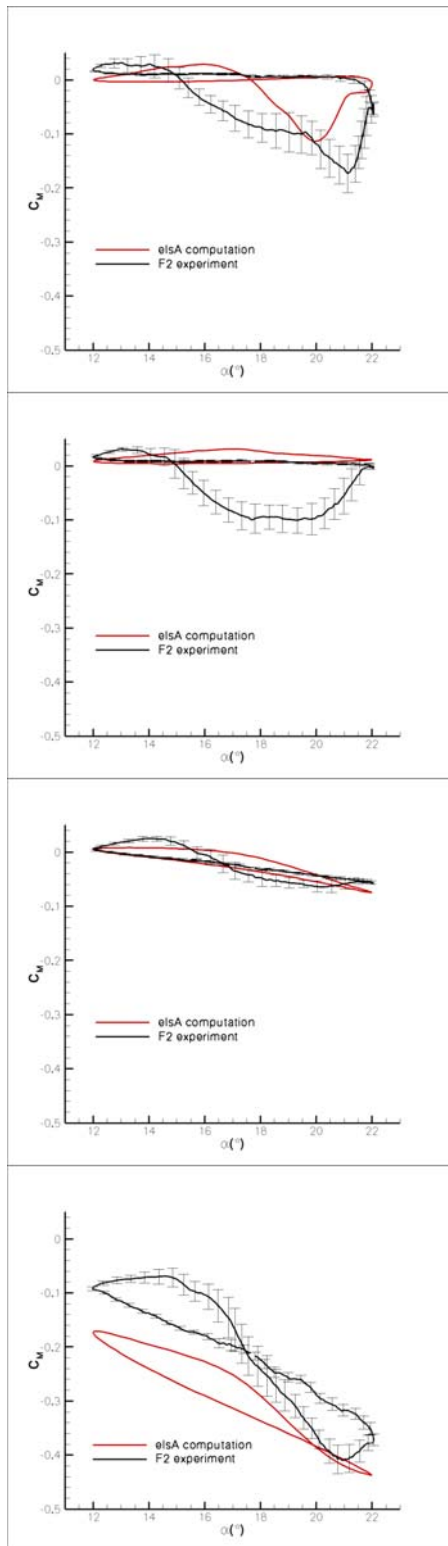
Figure 7: Evolution of the pitching moment coefficient for the 4 instrumented wing sections (from top to bottom: 50%, 80%, 95% and 99%) – SA computation

The underestimation of dynamic stall by the SA simulation is even clearer when considering the pitching moments (Figure 7). Contrary to the experimental data, the sections at r/R=80% to 95% only predict a counter clockwise pitching moment evolution with time, and therefore essentially no negative value of the pitching moment during the downstroke phase of the wing. Again, the effect of the tip vortex is correctly captured in the pitching moment simulations. It induces a larger rear loading at r/R=99% and therefore strong negative values and gradients of the pitching moment.

This underestimation of the dynamic stall of the wing is also clear in Figure 8, which gives an overview of the aerodynamic field around the wing in the part of the cycle when the computed dynamic stall is the most severe. The figure shows the friction contours and friction lines on the wing surface, as well as the field of turbulent viscosity in 5 cut planes: 4 chordwise planes along the pressure instrumented wing sections and a transversal plane a ¼-chord downstream of the wing. As already mentioned, the dynamic stall, which appears clearly for the section r/R=50%, does not reach the section r/R=80%.
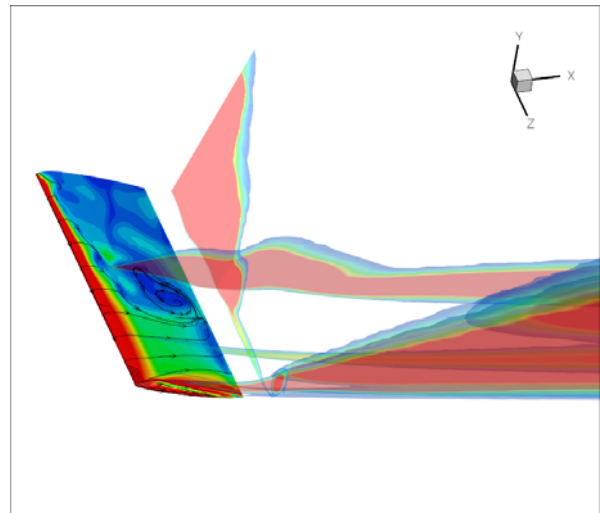

Figure 8: Global view of the aerodynamic field at α=18.5°↓ (SA computation)

k-ω turbulence model

The corresponding results obtained with the k-ω model are now considered. These simulations were initialized with the previous SA results for the conservative variables, the turbulent field being started with a prescribed turbulent to dynamic

viscosity ratio. Five cycles of oscillation have been computed with this turbulence model. The convergence of the lift coefficient over the revolutions for 2 selected sections, r/R=80% and r/R=99%, is presented in Figure 9, including the results from cycle 2 to cycle 5. Contrary to what was obtained with the SA model, deep dynamic stall is now predicted. As a result, although a very good time convergence is reached during the upstroke phase when the flow remains attached, cycle-to-cycle variations are obtained in the downstroke phase due to the shedding of dynamic stall vortices. According to the results obtained, the solution seems to vary between two states, one corresponding to the cycles 2 and 5, the other one corresponding to cycles 3 and 4. However, it is difficult to conclude since these cycles were run with different numbers of Newton iterations. Nevertheless, this variation between the cycles is very similar to that obtained in 2D dynamic stall, although the cycle-to-cycle variations in 3D have a smaller magnitude due to the additional degree of freedom provided to the flow-field.
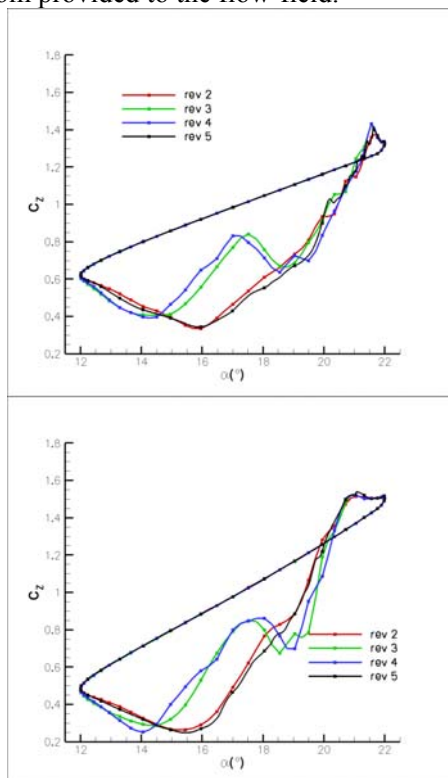
Figure 9: Convergence of the lift coefficient at two wing sections (r/R=80% - top and r/R=99% - bottom) with the k-ω model

The time convergence for the same sections is shown in Figure 10 for the pitching moment coefficient, and the results obtained are very consistent with the lift evolution.
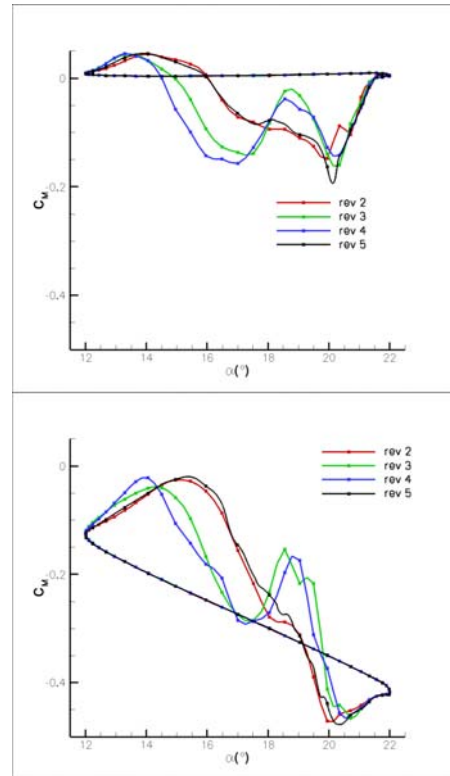

Figure 10: Convergence of the pitching moment coefficient at two wing sections (r/R=80% - top and r/R=99% - bottom) with the k-ω model

A comparison between computation and experiment for the lift coefficient is presented in Figure 11. The problems due to pressure uncertainties in the experiment are again noticeable, leading to large discrepancies between the computation and the experiment in the upstroke phase of the wing. Nevertheless, the k-ω computations provide a much better qualitative evolution of the dynamic stall effect on the whole wing, with a flow separation which extends much further outboard during the downstroke motion of the wing, although this dynamic stall seems to be slightly overestimated. This is also clear when considering the pitching moment (Figure 12) which shows a clockwise evolution with time for all sections up to 95% span. For this parameter, the elsA prediction is particularly good with respect to the current state-of-the-art. Finally, the suction effect of the tip vortex of the wing is also qualitatively well captured.
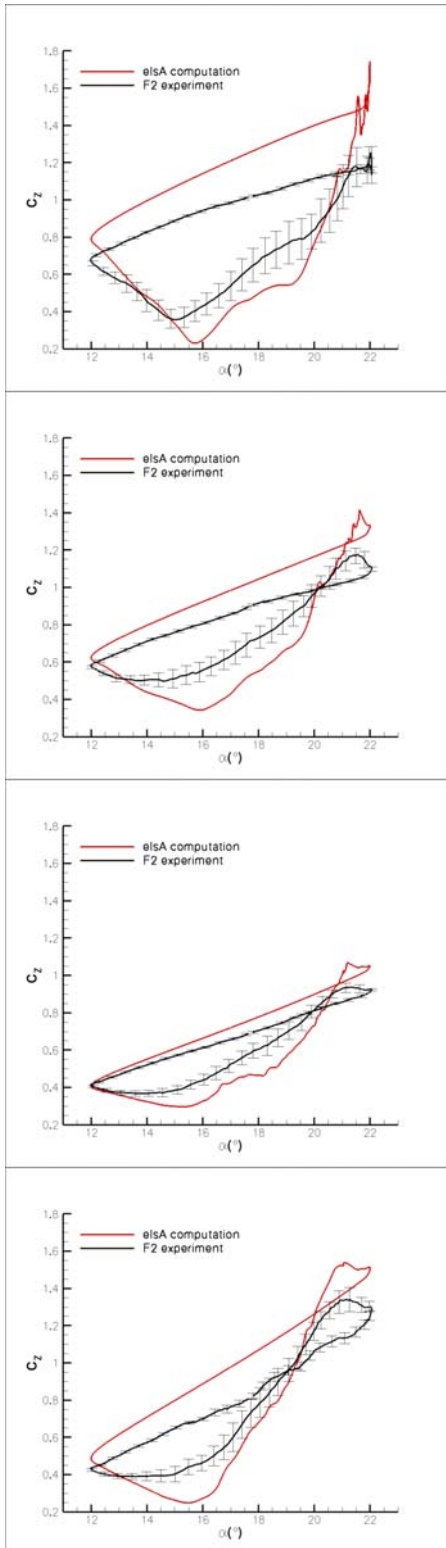
Figure 11: Evolution of the lift coefficient for the 4 instrumented wing sections (from top to bottom: 50%, 80%, 95% and 99%) – kω computation
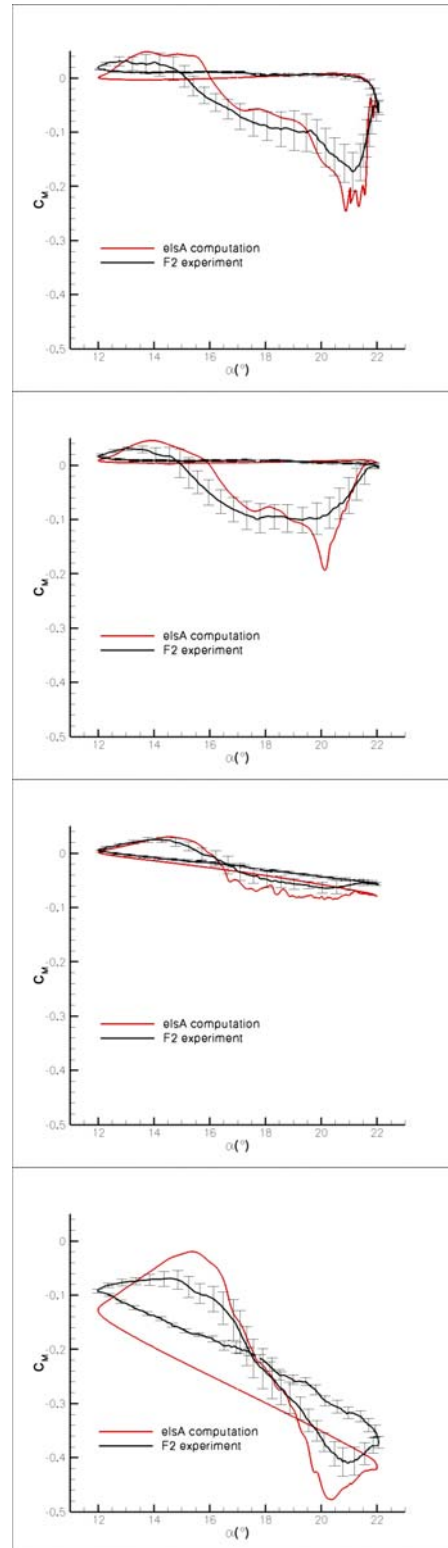
Figure 12 : Evolution of the pitching moment coefficient for the 4 instrumented wing sections (from top to bottom: 50%, 80%, 95% and 99%) – kω computation

The large extension of the separated flow region over the wing can also be observed on the overview of the flow field during the dynamic stall process (Figure 13 to Figure 16). As seen in Figure 13 and Figure 14, the dynamic stall vortex is first generated inboard and propagates towards the wing tip. This leading edge separation superimposes to a previous moderate trailing edge separation, leading to the impulsive shedding of dynamic stall vortices. Once massive flow separation is established (Figure 15), spanwise flow variations are weak, except at the very tip of the wing where flow separation is stopped by the tip vortex. The main 3-dimensionality which can be noted elsewhere comes from the wavy shape of the wake cross-section inside the separated region. The flow then reattaches progressively starting from the tip of the wing (Figure 16). Finally, when comparing the tip vortex computed with k-ω and SA turbulence models, the low level of turbulence in the vortex core with k-ω can be noted, in better agreement with the flow physics. The deficiencies of the SA model from this aspect are well-known, leading to the introduction of a rotational correction [14] not applied in the present work.
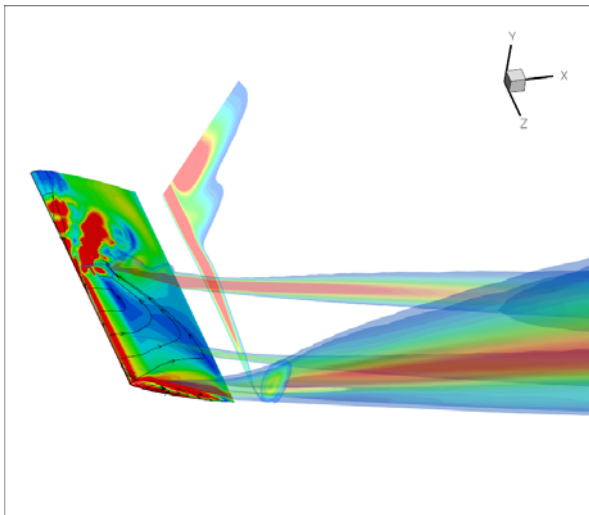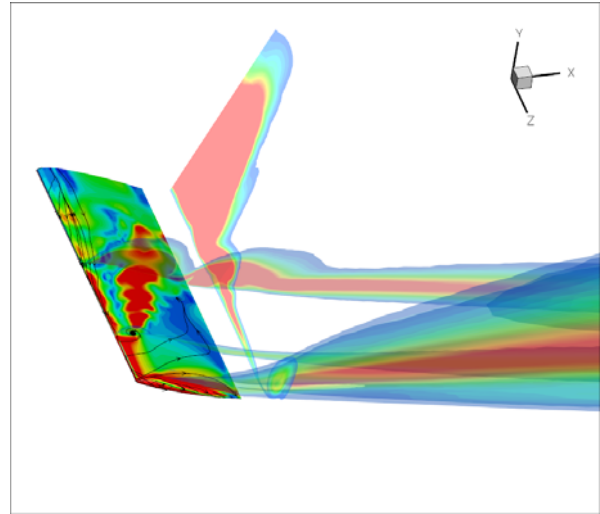

Figure 14: Global view of the aerodynamic field at α=21.6°↓ (kω computation)
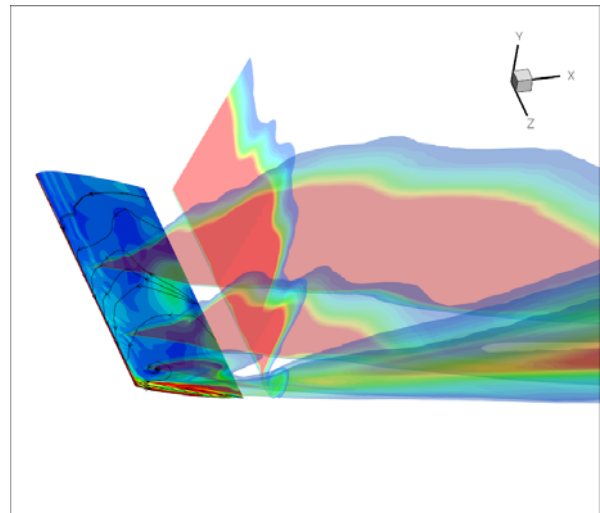
Figure 15: Global view of the aerodynamic field at α=18.5°↓ (kω computation)

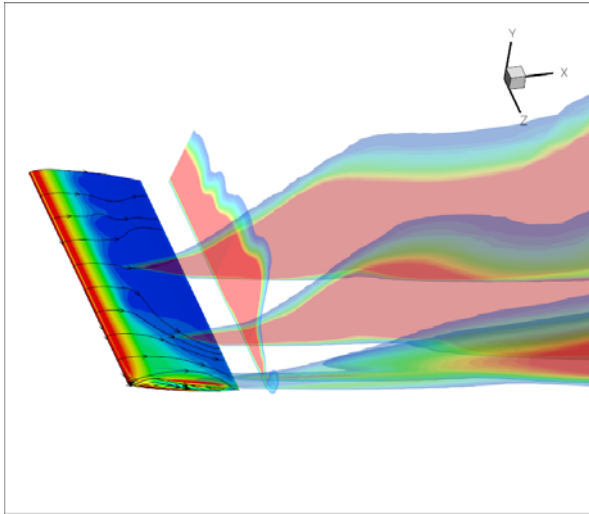**Figure 13: Global view of the aerodynamic field at α=22.0°↓ (kω computation)**

Figure 16: Global view of the aerodynamic field at α=14.5°↓ (kω computation)

The computed velocity field is compared with PIV experiment from Figure 17 to Figure 23. The phase-averaged PIV data is plotted in the bottom part of the figures, while the results obtained with the k-ω model are presented above with the boundary of the PIV window represented in black in order to make the comparison easier. A delay in the occurrence of dynamic stall for the elsA prediction can be noted from these comparisons (Figure 17). The same also applies during the reattachment process (Figure 23), with a delay in predicting the end of the dynamic stall cycle.
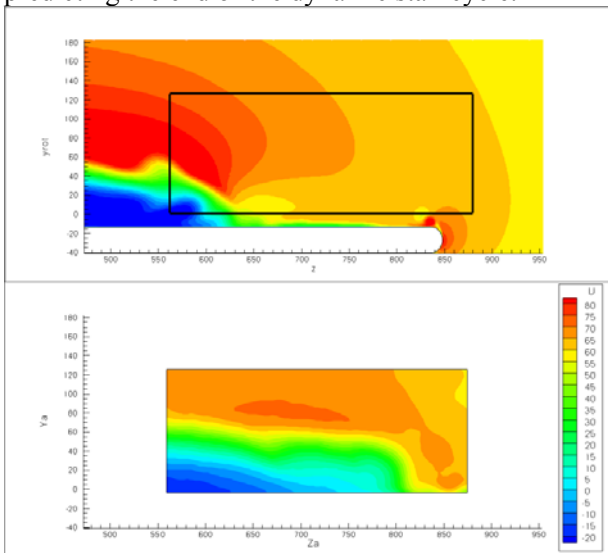

Figure 17: Comparison of computed and PIV longitudinal velocity component at x/c=50% and α=21.1°↓

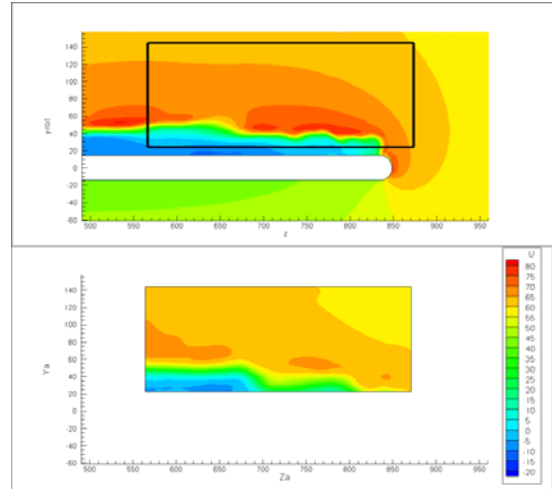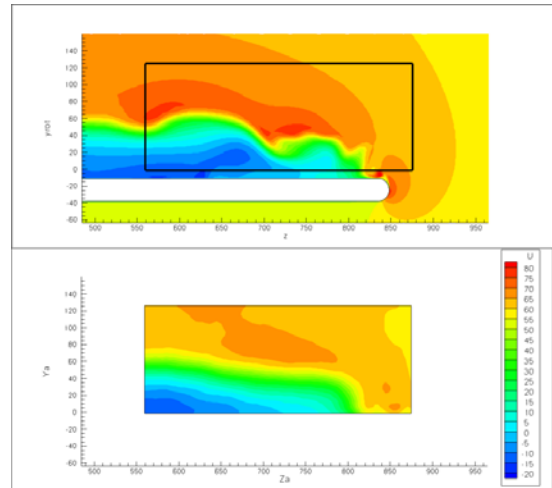**Figure 18: Comparison of computed and PIV longitudinal velocity component at x/c=25% and α=19.6°↓**

Figure 19: Comparison of computed and PIV longitudinal velocity component at x/c=50% and α=19.6°↓

In between, when the flow is fully separated over the upper surface of the wing, the correlation between the computed and the PIV velocity data is fairly good, as shown by the comparisons for α=19.6° during the downstroke. The axial velocity contours at x/c=25%, 50% and 75% (Figure 18, Figure 19 and Figure 20) reproduce most of the characteristics observed in the experiment. More particularly, the positive effect of the tip vortex to prevent the flow from separating in the tip region is very well captured by the numerical simulation, although its effect seems to be slightly underestimated at x/c=25% (Figure 18). A wavy shape of the velocity contours is also clearly

present in the computed results, consistently with the previous observations for the turbulent viscosity contours. It may come from a rolling up of the vorticity shed in the separated boundary layer. This behaviour is less obvious in the experiment, but a few elements tend to indicate that it is physically present in the flow field, as shown by the edge of the boundary layer at x/c=25% (Figure 18). Indeed, the phase-averaging process of the PIV data is likely to eliminate a large part of the high-frequency fluctuations. Finally, these figures also show a larger suction above the separated flow than in the PIV.
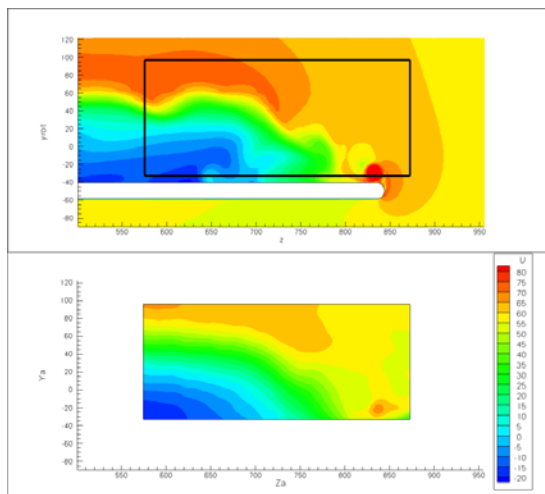

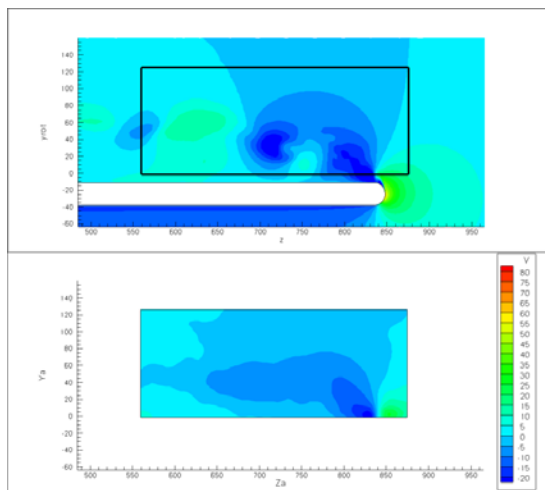**Figure 20: Comparison of computed and PIV longitudinal velocity component at x/c=75% and α=19.6°↓**

Figure 21 : Comparison of computed and PIV vertical velocity component at x/c=50% and α=19.6°↓

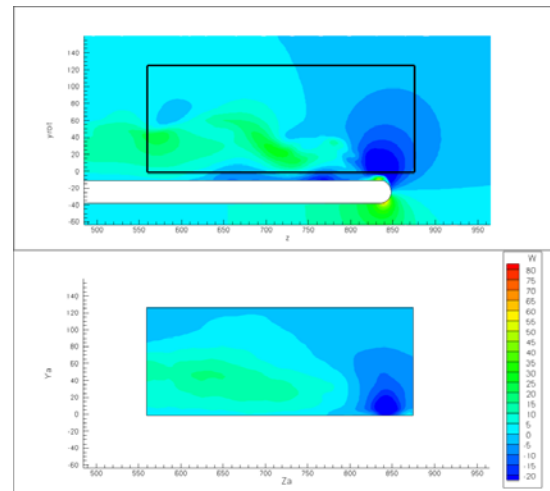**Figure 22 : Comparison of computed and PIV spanwise velocity component at x/c=50% and α=19.6°↓**

At x/c=50%, the correlation computation-experiment of the vertical and spanwise velocity components is also fairly good (Figure 21 and Figure 22). As for the longitudinal component, the experimental data appears to be smoother than the computed results, for the same reasons mentioned above.
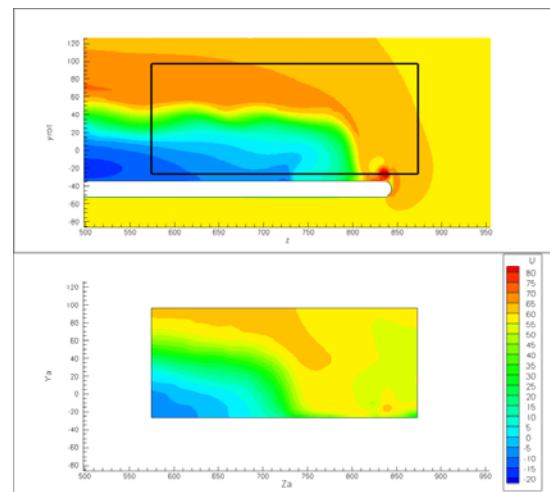

Figure 23: Comparison of computed and PIV longitudinal velocity component at x/c=50% and α=17.2°↓

A comparison of the numerical results predicted by the k-ω turbulence model with the LDV data measured for the wing section r/R=80% is presented from Figure 24 to Figure 28. Again, the experiment is plotted in the bottom part of the figures and the computations in the top. The edge

of the LDV measurement window is also plotted as black lines in the computed results. The selected phase angles of the wing pitch motion are close to those already selected for the comparisons with the PIV measurements. The first and the last comparisons, showing the longitudinal velocity contours at the beginning of the downstroke (α=21.5°) and in the middle of this downstroke phase (α=17.4°), confirm the delay in the occurrence of dynamic stall (Figure 24) and in the flow reattachment (Figure 28) already mentioned from the comparison with the PIV data.
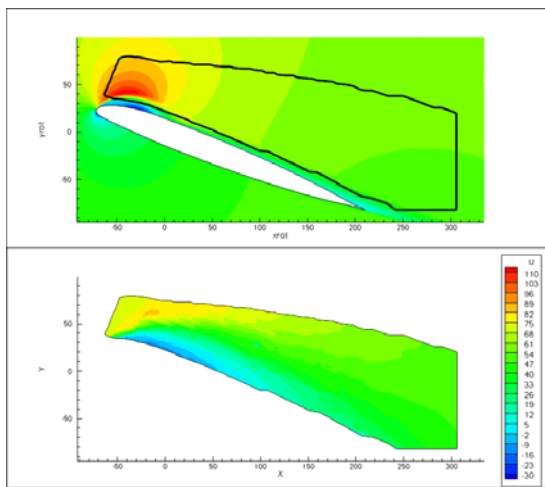

Figure 24: Comparison of computed and LDV longitudinal velocity component at r/R=80% and α=21.5°↓

During the dynamic stall process (α=19.1°), the correlation between the computed velocity field and the experiment is again fairly good (Figure 25 to Figure 27). The extent of separated flow is correctly predicted as can be seen from the contours of longitudinal velocity component (Figure 25). The vertical component of the computed velocity field shows discrete vortex structures which correspond to a shear layer in the experiment at the outer edge of the separating boundary layer (Figure 26). Again, the "high-frequency" details of the numerical simulation are smoothed out in the experimental data. This difference may also be explained by the phase-averaging process of the experiment. Finally, the spanwise velocity component (Figure 27) gives positive values (i.e. towards the wing tip) in the front part of the separated flow and negative values (i.e. towards the wing root) in the rear part of the

recirculation. This is to be related with the leading edge stall travelling from inboard to outboard of the wing and is probably linked to the influence of the tip vortex on the flow field. The maximum magnitude of these values of the spanwise velocity component appears to be larger in the computation than in experiment, for both positive and negative parts.
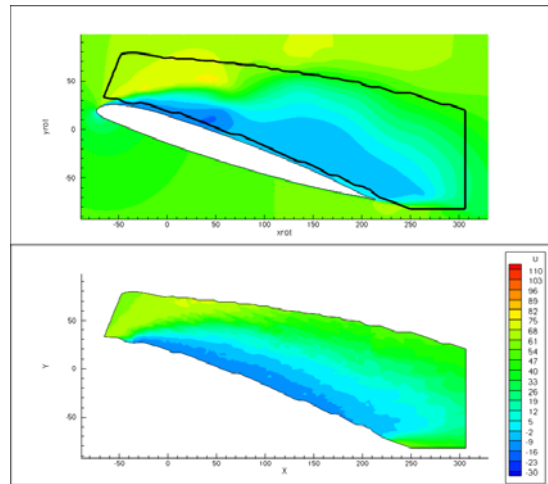

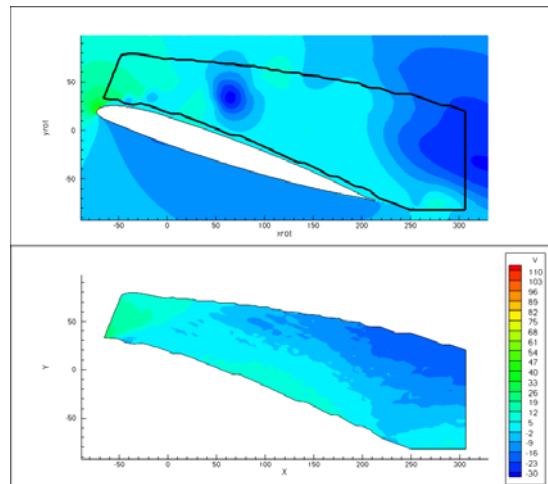**Figure 25: Comparison of computed and LDV longitudinal velocity component at r/R=80% and α=19.1°↓**

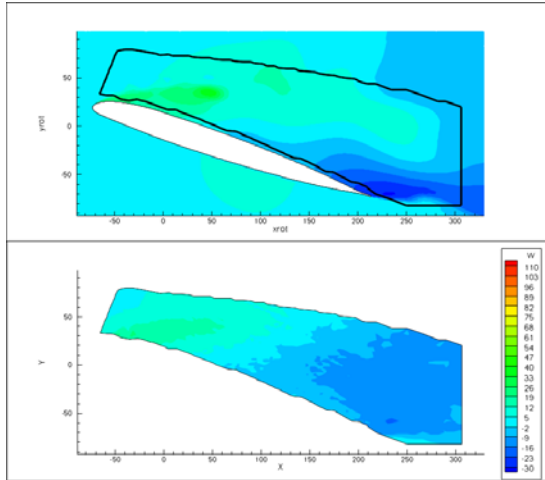**Figure 26: Comparison of computed and LDV vertical velocity component at x/c=50% and α=19.1°↓**

Figure 27: Comparison of computed and LDV spanwise velocity component at x/c=50% and α=19.1°↓

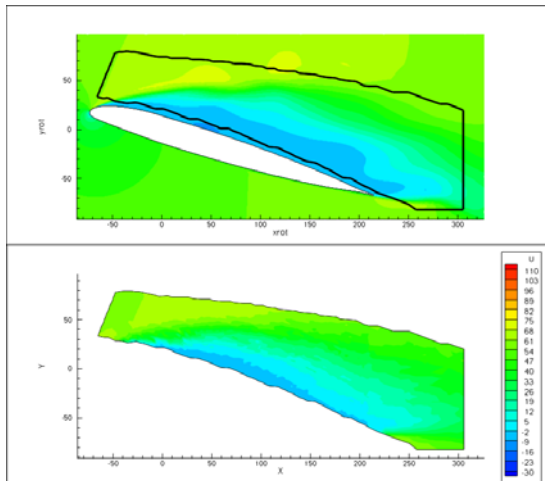**Figure 28: Comparison of computed and LDV longitudinal velocity component at r/R=80% and α=17.4°↓**

Conclusions

The work presented in this paper constitutes a first validation of unsteady RANS dynamic stall simulations for a 3D finite-span oscillating wing with the elsA CFD software at Onera. Two turbulence models were tested, the one-equation Spalart-Allmaras model and the two-equation k-ω model with Kok cross derivative terms and SST correction, for a single grid of approximately 17 Million of nodes. For this first validation, only fully-turbulent computations have been considered.

One deep stall configuration was computed, over 4 to 5 periods of oscillation of the wing. The results obtained with the SA model indicate a strong under-estimation of dynamic stall, very similarly to what was obtained in the simulation of dynamic stall for the 2D oscillating OA209 airfoil. On the contrary, the k-ω computations provide a simulation of dynamic stall in reasonable agreement with experiment, and qualitatively very good. A large discrepancy is obtained in the prediction of sectional lift coefficient, which is believed to be due to erroneous pressure measurements in the vicinity of the trailing edge of the wing. This will have to be investigated in the future. The prediction of pitching moment is in much better agreement with experiment, for the 4 instrumented sections of the wing, indicating that the 3-dimensionnal effects in the dynamic stall are fairly well simulated. This is confirmed by the comparison of the computed velocity field with LDV and PIV experimental data, which show a good qualitative description of the distribution of the velocity vector around the wing at several times during the stall process, and also a reasonably good quantitative agreement with experiment.

The "success" of this first simulation may be questionable when considering the difficulties encountered in the simulation of dynamic stall for similar 2D configurations [2]. Indeed, in these 2D simulations of the OA209 airfoil, it was found mandatory to account for the laminar-turbulent transition, even with the k-ω model, to capture dynamic stall, the fully turbulent computations giving only mild trailing edge separation in contrast with the deep stall found in the F2 experiment. A first explanation of this difference may lie in a more severe pitch configuration applied in the 3D tests. Finite-span effects actually reduce the effective angle of attack and the mean incidence had to be increased from 13° in 2D up to 17° in 3D in order to obtain similar stall phenomena in the central station of the wing. It is therefore possible that this 3D configuration is located slightly deeper in the stall regime than its 2D counterpart, thus rendering the numerical simulations easier. In any case, new computations taking into account laminar-turbulent transition are planned in the future in order to check its effect on the dynamic stall of the wing. Another possible explanation of the difference between 2D and 3D

dynamic stall may come from the boundary conditions of the 3D computation. As was seen in the analysis of the flow field, the leading edge separation starts from the wing root and propagates towards the tip. A 2D flow condition is applied in this section in the elsA simulation, and this condition may start the dynamic stall prematurely. The actual wing geometry had tapered root shape in order to allow the sweep angle to be varied from -30° to +30°, which was not considered in the present simulations. New computations will be run with this new geometry in order to check the effect of the root boundary condition in the simulation.

Acknowledgements

References

1. Le Pape, A., Pailhas, G., David, F., Deluc, J-M., "Extensive wind tunnel measurements of dynamic stall phenomenon for the OA209 airfoil including 3D effects", 33rd European Rotorcraft Forum, Kazan, Russia, September 2007.

2. Costes, M., Gleize, V., Le Pape, A., Richez, F., "Numerical investigation of laminar/turbulent transition effects on the dynamic stall of an oscillating airfoil", American Helicopter Society Specialist Conference on Aeromechanics, San Francisco, CA, January 23-25 2008.

3. Richter, K., Le Pape, A., Knopp, T., Costes, M., Gleize, V., Gardner, A., "Improved Two-Dimensional Dynamic Stall Prediction with Structured and Hybrid Numerical Methods", 65th American Helicopter Society Forum, Gravepine(TX), USA, 27-29 May 2009.

4. Le Pape, A., Costes, M., Richez, F., David, F., Deluc, J.M., "Experimental Study of Dynamic Stall Control using Deployable Leading-Edge Vortex Generators", 67th American Helicopter Society Forum, Virginia Beach (VA), 3-5 May 2011.

5. Joubert, G., Le Pape, A., Huberson, S., "Numerical study of flow separation control over a OA209 airfoil using deployable vortex generator", 49th AIAA Aerospace Sciences Meeting AIAA-2011-1044 , 2011.

6. Ekaterinaris, J.A., "Numerical investigation of dynamic stall of an oscillating wing", AIAA Journal, Vol. 33, No. 10, pp. 1803-1808, 1995.

7. Spentzos, A., Barakos, G., Badcock, K., Richards, B., Wernert, P., Schreck, S., Raffel, M., "CFD investigation of 2D and 3D dynamic stall", AHS 4th Decennial Specialist's Conference on Aeromechanics, San Francisco, California, January 21-23, 2004.

8. Spentzos, A., Barakos, G.N., Badcock, K.J., Richards, B.E., Coton, F.N., Galbraith, R.A., Berton, E., Favier, D., "Computational fluid dynamics study of three-dimensional dynamic stall of various planform shapes", Journal of Aircraft, Vol. 44, No. 4, pp. 1118-1128, July-August 2007.

9. Sitaraman, J., Datta, A., Baeder, J., Chopra, I., "Coupled CFD/CSD Prediction of Rotor Aerodynamic and Structural Dynamic Loads for Three Critical Flight Conditions," ERF, Florence, Italy, Sept. 2005.

10. Potsdam, M., Yeo, H., and Johnson, W., "Rotor Airloads Prediction Using Loose Aerodynamic/Structural Coupling," AIAA Journal of Aircraft, Vol. 43, No. 3, May-June 2006, pp. 732-742.

11. Sankaran, V., Potsdam, M., Wissink, A., Datta, A., Jayaraman, B., and Sitaraman, J., "Rotor Loads Prediction in Level and Maneuvering Flight Using Unstructured-Adaptive Cartesian CFD," AHS 67th Annual Forum, Virginia Beach, VA, May 2011.

12. Biedron, R. and Lee-Rausch, E., "Computation of UH- 60A Airloads using CFD/CSD Coupling on Unstructured Meshes," American Helicopter Society 67th Annual Forum, Virginia Beach, VA, May 3-5, 2011.

13. Gazaix M., Jolles A., Lazareff M., "The elsA object-oriented computational tool for industrial application", 23rd ICAS Conference, September 2002.

14. Duraisamy, K., Baeder, J.D. "High resolution wake capturing methodology for hovering rotors", Journal of the AHS, Vol. 52, No. 2, pp. 110-122, April 2007.